Effects of phosphate on biotite dissolution and secondary precipitation under conditions relevant to engineered subsurface processes†

Lijie Zhang [iD] [a], **Doyoon Kim** [a], **Yongman Kim** [b], **Jiamin Wan** [b] **and Young-Shin Jun** [iD] *[a]

[a]*Department of Energy, Environmental and Chemical Engineering, Washington University, One Brookings Drive, Campus Box 1180, St. Louis, MO 63130, USA. E-mail: ysjun@seas.wustl.edu; Web: http://encl.engineering.wustl.edu/ Fax: +1-(314)-935-7211; Tel: +1-(314)-935-4539*

[b]*Energy Geosciences Division, Lawrence Berkeley National Laboratory, Berkeley, CA 94720, USA*

Brine–mica interfacial interactions affect both the caprock integrity and the fate and transport of reactive fluids at deep subsurface sites. Phosphate naturally exists at low concentration in subsurface brines, and its concentration can be increased significantly during energy-related engineered subsurface processes. However, our understanding of the influence of phosphate on brine–mica interactions is limited, especially under subsurface conditions. Here, biotite dissolution experiments were conducted without and with phosphate (0.1, 1, and 10 mM) at 95 °C and 102 atm CO_2. Compared to the control, 0.1 mM, and 1 mM phosphate systems, biotite dissolution was four times higher with 10 mM phosphate. Despite the dissolution differences, in all the phosphate systems, phosphate interacted with Al and Fe sites in biotite, forming surface complexation and precipitating

as Fe- or Al-bearing minerals on surfaces and in solutions. Consequently, aqueous Fe and Al concentrations became lower with phosphate than in the control experiments. In addition, the biotite basal surfaces became more hydrophilic after reaction with phosphate, even at 0.1 mM, mainly from phosphate adsorption. This study offers new information on how phosphate-containing brine interacts with caprocks and on the consequent wettability changes, results that can benefit current and future energy-related subsurface engineering processes.

1. Introduction

Energy-related subsurface operations, such as geologic CO_2 sequestration (GCS) and CO_2-enhanced oil/gas recovery, are promising strategies to mitigate global warming and meet energy demands.[1,2] Both strategies include CO_2 injection at subsurface sites,[1,3] where the temperature and pressure can range between 31–110 °C and 73.8–600 atm, respectively.[4-6] After injection, CO_2 stays in its supercritical phase ($scCO_2$) or dissolves in brine, forming H_2CO_3 and HCO_3^- aqueous species and releasing H^+. A caprock layer at the site serves as a seal, hindering the upward movement of injected CO_2. The efficacy of the layer is largely governed by capillary pressure.[7] As denoted in

$$P_c = P_{CO_2} - P_w = \frac{2\gamma_{wc}\cos\theta}{R}$$

the Young–Laplace equation, , the capillary pressure (P_c), *i.e.*, the pressure difference between CO_2 pressure (P_{CO_2}) and water pressure (P_w), is dependent on the $scCO_2$–brine interfacial tension (γ_{wc}), pore radius (R), and wettability (θ). During GCS, to store CO_2 in reservoir rock pore spaces initially occupied by brine, the CO_2 pressure should exceed the capillary pressure and displace the brine; later, brine can again substantially replace CO_2, leaving some trapped in the pore spaces by capillary forces.[8-10] On the other hand, if the CO_2 pressure exceeds the capillary pressure, the sealing of the caprock layer fails in which case CO_2 will leak.

Owing to the high temperature, pressure, and salinity in subsurface sites, and to the low initial pH induced by injected CO_2, dissolution of reservoir or caprock minerals and secondary mineral precipitation can occur.[11-17] Mica is a group of abundant minerals in caprocks at subsurface sites, with a mass fraction of about 30% in the Sleipner shales in Norway and 10–33% in the Venture gas field in Canada.[18,19] Recent studies report that mica can react with

scCO₂-saturated brine, subsequently affecting the geophysical properties of caprocks and creating CO_2 leakage pathways.[11,14,15,20-22] Such interactions between brine and minerals may alter the porosity, permeability, or wettability of the rocks related to the capillary pressure, thus influencing the sealing of the caprock layer.[17] Because the integrity of the caprock layer is essential to the long-term subsurface storage of CO_2, a better understanding of the effects of brine chemistry on chemical reactions of mica under relevant conditions is needed to ensure safe and efficient subsurface operations.

At subsurface sites, both inorganic and organic ligands are abundant in brine.[13,23-25] The effects of organic ligands, such as acetate and oxalate, on mineral dissolution have been investigated under subsurface conditions. For example, acetate slightly inhibited the dissolution of feldspar and biotite, however, oxalate significantly enhanced biotite dissolution.[14,26]Among inorganic ligands, phosphate is reported in subsurface brine with concentrations between 0.5–20 µM.[25] It is well known that phosphate has a strong surface complexation capacity under ambient conditions and can adsorb onto mineral surfaces, such as aluminum or iron (hydr)oxides.[27-29] In addition, phosphate can precipitate with aluminum or iron ions in acidic solutions or oils.[30,31] Both the adsorption and precipitation triggered by phosphate may disturb the water–mineral equilibrium and cause the minerals to dissolve and undergo phase transformation. Further, phosphate can interact with mica minerals, which have more complicated structures than metal (hydr)oxides.

The phosphate surface complexes mentioned above have several configurations, such as monodentate mononuclear, bidentate mononuclear, or bidentate binuclear, depending on experimental conditions such as ionic strength and pH.[27,28,32-34] The configurations of surface complexes have different

effects on mineral dissolution.[35–38] For example, monodentate and bidentate mononuclear complexations are expected to promote mineral dissolution by polarizing and weakening the bonds between the surface cations and mineral lattice, whereas bidentate binuclear complexation can inhibit mineral dissolution as a result of the large activation energy required to release the two metal centers and the lack of surface protonation at uncharged binuclear sites.[35,37–39] The influenced dissolution will further impact the saturation conditions of potential minerals in the system, thus affecting secondary precipitation. Despite the importance of surface complexation, the influences of adsorbed phosphate on mica minerals on their consequent dissolution and secondary mineral precipitation under subsurface conditions have not been evaluated.

In addition to naturally occurring phosphate, phosphonate-based scale inhibitors, such as diethylenetriaminepenta(methylene phosphonic acid) (DTPMP), are widely used in subsurface engineering processes, such as conventional and unconventional oil/gas production or geothermal operations.[40,41] The average concentration of phosphonate scale inhibitor is about 0.023 wt% (0.5 mM). They contain two or more phosphonate functional groups with a strong complexation capability,[42] similar to phosphate, which can also affect mineral dissolution and secondary precipitation.[41] Furthermore, microorganisms or oxidizing biocides used to control microbiological growth in hydraulic fracturing can degrade phosphonates into orthophosphate, increasing the concentration of orthophosphate to around 1–2 mM.[43,44] Hence, an investigation of the effects of phosphate on brine–mica interactions can be a good starting point to better understand the effects of naturally occurring inorganic ligands and provide new information about the potential effects of phosphonate-based scale inhibitors in energy-related subsurface operations.

Moreover, chemical reactions between phosphate and mica, including adsorption, dissolution, and secondary precipitation, can cause wettability changes in mica by changing the physico-chemical properties of surfaces.[15] As we described earlier, the wettability of mineral surfaces, usually expressed by contact angles (θ), can largely determine the mobility, migration, and distribution of reactive fluids, and thus it is an important parameter for engineered subsurface operations. The hysteresis in the contact angle can also be a good indicator of the residual trapping capacity of CO_2, both during injection and post-injection.[45] In our previous study,[15] we found that higher salinity can enhance biotite dissolution, inducing a rougher surface, more surface charge, and a higher density of surface hydroxyl groups. Consequently, the biotite became more hydrophilic under subsurface conditions. Likewise, the interactions between phosphate and mica minerals may change the mineral surface morphology and mineralogy, leading to wettability alteration. Nevertheless, how phosphate affects mica wettability is still unknown.

Therefore, the objective of the present study is to provide mechanistic understanding of the physicochemical effects of phosphate on biotite dissolution and secondary precipitation, and to link chemical reactions with the wettability change of biotite under high temperature and high pressure (95 °C and 102 atm CO_2) conditions. Biotite was chosen as a model caprock mineral, as in previous studies.[14,15] For the first time, this study identifies the significant roles of phosphate in brine–mineral interactions and the subsequent distinctively enhanced biotite wettability. Ultimately, the explicit information of physical chemistry of phosphate in a wide range of concentrations obtained from this single-mineral system can be useful for better interpreting complex reaction systems, and can also benefit other current and future engineered subsurface processes in addition to GCS.

2. Experimental

2.1 Minerals and chemicals

The composition of biotite purchased from Ward's Natural Science was analyzed with X-ray fluorescence (XRF) and found to be $K_{0.91}Na_{0.08}Ca_{0.05}Mg_{1.72}Mn_{0.06}Fe_{1.12}Ti_{0.12}Al_{1.00}Si_{2.98}O_{10}(F_{0.51}(OH)_{0.49})_2$ (Table S1, ESI†). Biotite flakes with a thickness of 80 ± 10 μm (measured by a Vernier caliper) were cleaved along the {001} basal planes with a razor blade and cut into 2.0 cm × 0.8 cm rectangles. The biotite flakes were sonicated successively in acetone, ethanol, and isopropanol, each for 5 minutes, to remove organic contaminants, then washed with deionized (DI) water (resistivity > 18.2 MΩ cm, Barnstead ultrapure water systems). Finally, they were dried with high purity nitrogen gas for high temperature and high pressure experiments.

All chemicals used in this study were ACS grade or higher. At subsurface sites, the brine usually has a salinity between 0.01–2.2 M.[23,46-48] Hence, a background salinity of 1 M NaCl was used to simulate subsurface conditions. To examine the effects of phosphate, initial phosphate concentrations of 0 (control), 0.1, 1, and 10 mM were prepared by adding disodium phosphate to 1 M NaCl solution. The two relatively higher concentrations (1 and 10 mM phosphate) were chosen to facilitate observations by laboratory instruments (*e.g.*, Fourier transform infrared spectroscopy). These concentrations can also be found in localized environments or subsurface sites where phosphonates degrade and consequently release a high amount of phosphate.

2.2 High temperature and high pressure reactions

Biotite dissolution experiments were conducted in a 300 mL high temperature and high pressure reactor (Parr Instrument Co., IL, Fig. S1, ESI†) used in our previous studies.[11,14,15,49,50] Generally, at subsurface sites, the temperature and pressure depend on the depth, with the relationships $T(°C) = 15 + 33d$ and $P(atm) = 1 + 100d$ (d is depth in kilometers).[51] We used a pressure of 102 atm CO_2 to simulate field site pressure at a depth of about 1 km, which is within the depth range of subsurface sites used for engineered operations. However, the experimental temperature was 95 °C, which was higher than the temperature at 1 km depth. By using a relatively high temperature to trigger fast reactions, we made observations available within a reasonable experimental time and could also compare the data with previous studies conducted in a similar temperature range.[11,14,15,49,50] The pH of the control system was 3.16, assuming equilibrium at 95 °C and 102 atm of CO_2, as calculated by Geochemist's Workbench (GWB, Release 8.0). The

relevant thermodynamic calculations can be found in S2 in the ESI.† Thus, the initial pH of the solutions with phosphate was adjusted prior to CO_2 injection, which gave the systems the same pH value as the control system without phosphate (pH = 3.16 at 95 °C and 102 atm of CO_2). The pH adjustment was conducted using diluted trace metal hydrochloric acid (HCl, BDH) and sodium hydroxide (NaOH, BDH). The addition of HCl and NaOH did not much affect the ionic strength due to the pre-existing high concentration of NaCl (1 M) used. The experimental conditions mimicked the GCS conditions in the early period of CO_2 injection and at injection zones close to the injection well. Biotite flakes were reacted in the prepared solutions for the desired time intervals (3, 8, 22, 44, 70, and 96 h). After reactions, the solutions were filtered through 0.2 μm polypropylene membranes and acidified in 1% trace metal nitric acid. The aqueous solutions were analyzed with inductively coupled plasma-optical emission spectrometry (ICP-OES, PerkinElmer Optima 7300 DV) for the dissolved concentrations of biotite components (K, Al, Fe, Si, and Mg), and with ion chromatography (IC) for the residual phosphate concentration in the solutions. The final pH (96 h reaction time) was calculated by GWB, taking the ICP-OES and IC results as inputs for thermodynamic calculations.

2.3 Characterization of reacted biotite samples

The reacted biotite flakes were rinsed with DI water as soon as they were taken from the reactor, and dried with high purity nitrogen gas. The rinsed reacted biotite flakes were mounted onto steel pucks and placed on sample stage, and then measured with atomic force microscopy (AFM, Nanoscope V Multimode SPS, Veeco) for surface morphology. AFM measurements were conducted under ambient conditions in contact mode. Areas of 50 μm by 50 μm were scanned at a rate of 0.999 Hz and a deflection set point of 1.975 V, using nonconductive silicon nitride probes (tip radius of 10 nm, DNP-S10, Bruker). The collected AFM images were analyzed with Nanoscope software (v7.20). Root-mean-square surface roughness (R_q) is defined

as $$R_q = \sqrt{\frac{1}{L}\int_0^L \left|Z^2(x)\right|dx}$$ [52] where $Z(x)$ is a function that describes the surface profile analyzed in terms of the height (Z) and position (x) of the sample over the evaluation length L. We used this definition as an indicator of surface roughness. The reported roughness was calculated from at least four obtained AFM images for each sample.

To prepare samples for scanning electron microscopy-energy dispersive X-ray spectroscopy (SEM-EDX, Nova NanoSEM 230), biotite flakes reacted with 10 mM phosphate for 70 h were collected, carefully rinsed, and dried as before prior to the measurements. The samples were coated with AuPd, and a 10.00 kV electron accelerating voltage was used for the measurements.

High resolution-transmission electron microscopy (HR-TEM, JEOL-2100F) was also used to characterize precipitates in solutions and on biotite basal surfaces after 22 h and/or 96 h reactions. For imaging precipitates on biotite basal surfaces, biotite debris with secondary precipitates was detached from sample surface using sonication in ethanol for 5 min and a droplet of the suspension was placed on a Formvar/carbon coated-Cu TEM grid (Electron Microscopy Science, PA). To image precipitates in the solution, the solution after reaction was centrifuged at 5000 rpm for 5 min, and the supernatant containing dissolved ionic species was discarded. DI water was then added to the centrifuge tube, which was centrifuged for another 5 min. This process was repeated five times, until no ionic species were detected in the supernatant solutions. A droplet was then taken from the bottom of the solution (containing only particles formed during the reactions) and placed on a TEM grid. In this way, all detectable ionic species were removed to prevent unexpected precipitation during the drying process, which might affect TEM characterization. To identify the phase of the secondary precipitates formed during high temperature and high pressure reactions, we obtained the lattice fringes, electron diffraction patterns, and elemental compositions by energy dispersive X-ray spectroscopy during TEM measurements.

Under ambient conditions, using a contact angle analyzer (Surface Electro Optics, Phoenix 300), contact angles (CA) were measured with DI water for biotite samples reacted in the control, 0.1 mM, 1 mM, and 10 mM phosphate systems at 95 °C and 102 atm of CO_2 for 70 h (S2 in the ESI‡). Additional biotite flakes with dimensions of 2.5 cm × 2.5 cm × 80 μm were prepared and reacted in control and 10 mM phosphate solutions for 70 h. The reacted biotite flakes were then measured for contact angles with an customized apparatus (Fig. S2, ESI‡) under high temperature and high pressure.[15] The

measurement conditions were kept at 48 ± 1 °C and 102 atm of CO_2, to mimic subsurface conditions and to have a low enough temperature to avoid additional reactions during measurements. As confirmed in our recent study using AFM, there was no discernible alteration of biotite basal surfaces under these conditions.[15] Therefore, the CA differences resulted solely from the pretreatment reactions. Both static CA and dynamic CA were measured using a captive drop method by passing scCO$_2$through a needle to form a droplet on the mineral surface in an upside-down chamber (the detailed measurement process can be found in S3 in the ESI†). During dynamic CA measurements, scCO$_2$ was slowly added to or withdrawn from the droplet on the sample surface through the needle tip located near the sample surface. This process was recorded by a camera. For each sample, five to eight measurements were performed, and CAs of scCO$_2$ were directly measured from the images obtained with a high-resolution time-lapse camera (6.2 Megapixel, Nikon D7000). Water CAs were obtained by subtracting the scCO$_2$ contact angles from 180 degrees, and the average CAs of the water phase were reported. The length of the contact line, *i.e.*, the ternary phase line among biotite, CO_2, and brine, was measured at the last moment of the CO_2receding process, just before CO_2 detached from the needle (Fig. S3, ESI†).

2.4 Fourier transform infrared (FTIR) spectroscopy analyses of phosphate complexation

Attenuated total reflectance (ATR)-FTIR spectra were collected using a Thermo Scientific Nicolet iS10 spectrometer with a horizontal Ge ATR crystal to investigate the types of phosphate–biotite surface complexes. Biotite was ground, and particles with an average size of about 100 nm were collected (S1 in the ESI†). The particles were suspended in ethanol, deposited onto the Ge crystal, and allowed to dry.[14] Solutions were prepared of (a) 1 M NaCl, (b) 1 M NaCl + 1 mM phosphate, and (c) 1 M NaCl + 10 mM phosphate. All three solutions had a pH of 3.16, which is the initial pH under conditions of 95 °C and 102 atm of CO_2. Next, 1 mL of the prepared solution was added to the crystal and allowed to contact the dried biotite particle film. An average of 400 scans at a resolution of 1 cm^{-1} was used. To obtain phosphate

complexation information, the spectrum of biotite contacting solution (a) was used as a background and subtracted from the spectra of biotite contacting solutions (b) and (c). The observed spectra were normalized by the highest absorbance in the region of interest (1200–950 cm^{-1}) and the spectrum of 10 mM phosphate sample was offset to show the features of the two spectra.

3. Results and discussion

3.1 Concentration-dependent and element-specific effects of phosphate on biotite dissolution

The effects of phosphate on biotite dissolution under conditions relevant to subsurface environments are phosphate concentration-dependent and element-specific, as shown in Fig. 1. Due to similar extents of ion-exchange reactions, the concentrations of K$^+$ in the solutions were almost the same for all reaction systems (0, 0.1, 1, and 10 mM phosphate) after biotite dissolution within 96 h (detailed explanation can be found in S2 in the ESI†). On the other hand, after reaction with 10 mM phosphate, the concentrations of Si and Mg were about 3–4 times higher than in the control experiments, while the effects of 1 mM phosphate were not discernible. Unlike the Si and Mg cases, after about 20 h, the aqueous concentrations of Al were lower in the 1 mM and 10 mM phosphate systems than in the control system. As for the evolution of aqueous Fe, in the early stage (*i.e.*, reactions time shorter than 44 h), the concentration was higher in the 10 mM phosphate than in the control. In the later stage, reaction times of 44 h and longer, the concentrations of Fe became lower for 1 mM and 10 mM phosphate systems than that in the control. At an even lower phosphate concentration of 0.1 mM, after 44 and 70 h reaction, while the aqueous Si and Mg concentrations were close to those of the control, lower Fe and Al concentrations were still observed, further suggesting the concentration-dependent and element-specific effects of phosphate.
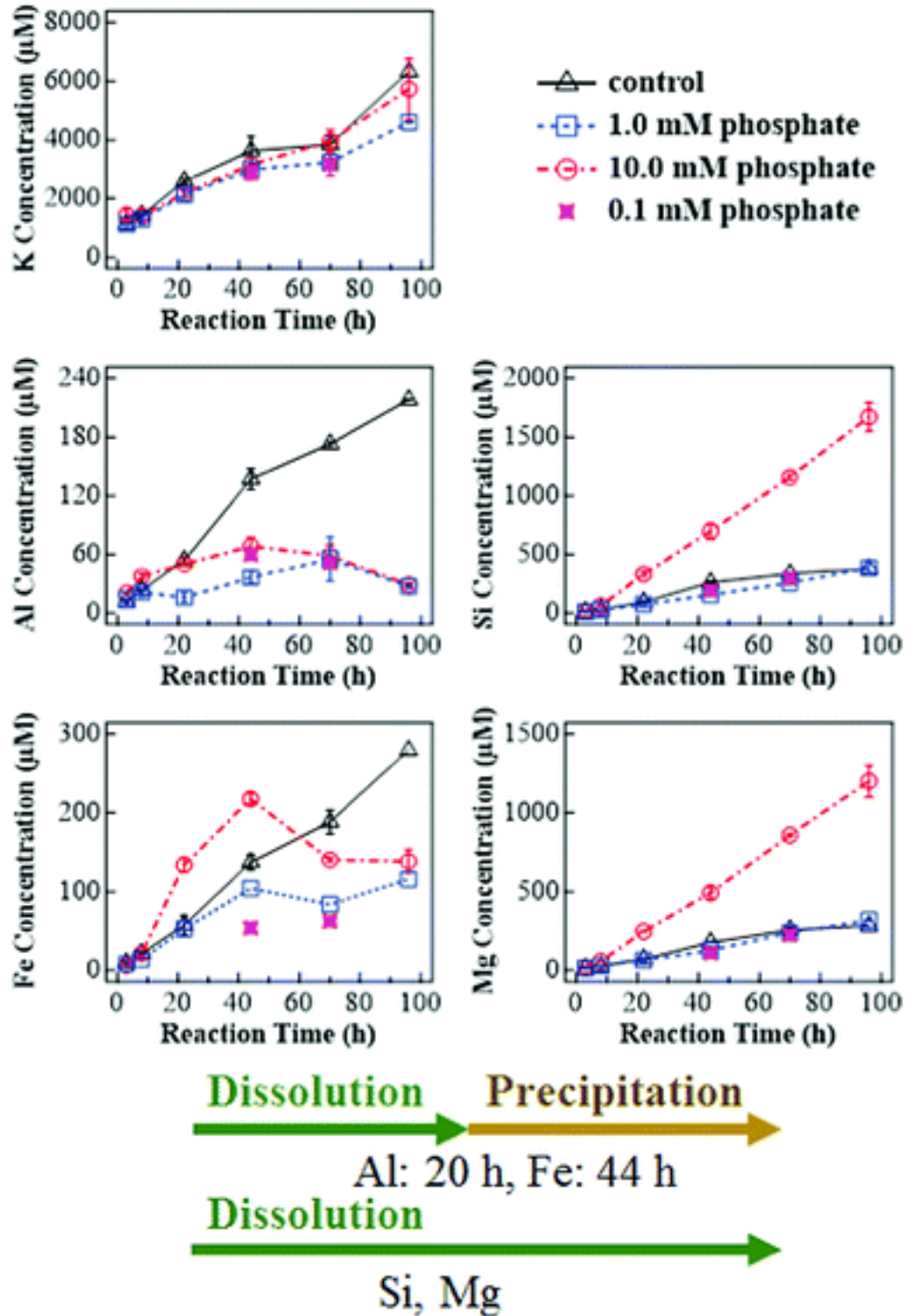
Fig. 1 Aqueous concentrations of K, Al, Si, Fe, and Mg from biotite dissolution at $T = 95\ °C$ and $P_{CO_2} = 102$ atm 1.0 M NaCl and initial pH of 3.16 with 0, 0.1, 1, and 10 mM phosphate. Error bars are the standard deviation of The dominant reactions over time in the presence of phosphate are indicated at the bottom of the figure.

To mechanistically explain the effects of phosphate on the evolution of framework cations, three aspects were considered: first, aqueous complexation between phosphate and cations can increase apparent solubility, enhancing biotite dissolution. However, the UV-Vis absorbance of phosphate aqueous complexation was weak (Fig. S4, ESI†). Therefore, aqueous complexation was not the main mechanism of the phosphate effects. Second, surface complexation can play a role. Phosphate can interact with surface Fe and Al sites through bidentate mononuclear or monodentate mononuclear complexation, promoting their release into solutions, and subsequently promoting the dissolution of Si and Mg, with stronger surface complexation in the presence a higher phosphate concentration. However, the aqueous Fe and Al concentrations were low at later reaction stages with phosphate. Hence, in addition to surface complexation, secondary precipitation was considered because the precipitation of Fe- or Al-bearing secondary phases can lower the aqueous concentrations of Fe and Al. Note that the ion concentrations shown in Fig. 1 measured by ICP-OES are the net concentrations from dissolution and secondary precipitation. We assumed that 0.1 mM and 1 mM phosphate did not greatly promote biotite dissolution, and we further assumed that 10 mM phosphate promoted the release of Al and Fe, as it did for Si and Mg. After longer reaction times (44 h for Fe and 22 h for Al), secondary precipitation became dominant. Significant secondary precipitation of Fe- or Al-bearing minerals in the solution or on biotite surfaces could explain their observed lower aqueous concentrations. Secondary mineral precipitation, removing Fe and Al cations from the solution, can further promote forward mineral dissolution. Therefore, we postulated that surface complexation and secondary precipitation could be mechanisms responsible for the concentration-dependent and element-specific effects of phosphate.

Thermodynamic calculations show that after 22 h and 96 h reactions, the 1 mM and 10 mM phosphate systems are saturated with Fe- and Al-bearing minerals, and that the saturation indices increase as reaction continues (Table S2, ESI†), consistent with our hypotheses. To support the mechanisms of the phosphate effects on aqueous cation evolutions, we conducted further investigations on surface properties using AFM.

3.2 Effects of phosphate on the surface morphological changes of biotite

The AFM images in Fig. 2 show that biotite basal surface morphological changes over time were significantly affected by 10 mM phosphate, while samples reacted with 1 mM phosphate had morphology similar to the control samples. Consistent with our recent reports, we observed the formation of cracks on biotite basal surfaces caused by ion-exchange reactions and CO_2 intercalation after 22 h reaction in the control experiment.[14,49] With 1 mM phosphate, cracks formed as in the control samples, with similar crack depths (Fig. S5, ESI†). However, with 10 mM phosphate, cracks were observed within 8 h reaction (Fig. 2C), indicating that 10 mM phosphate promoted biotite dissolution. Moreover, as AFM images show (Fig. 2C), biotite basal surfaces were significantly covered by secondary precipitates after reaction with 10 mM phosphate, increasing the roughness of the biotite basal surfaces. For example, after 22 h reaction, the root-mean-square surface roughness values given by AFM measurements of scan areas of 50 μm × 50 μm were 4.7 ± 1.4 nm, 7.0 ± 1.8 nm, and 26.8 ± 3.2 nm for the control, 1 mM phosphate, and 10 mM phosphate samples, respectively. Due to the high surface roughness resulting from coverage by a large quantity of secondary precipitates with 10 mM phosphate, AFM could not resolve the surface features clearly. Thus, a complementary tool, SEM, was used to clearly show the biotite basal surface after reaction with 10 mM phosphate for 70 h. As seen in the inset in Fig. 2C_70 h as well as Fig. 4C, the biotite surface was covered by a thin film of amorphous phases underneath round particles. The diameters of the particles were up to 200 nm. EDX analysis showed that the round particles were more abundant in Fe and Al than the raw biotite material (Fig. S6, ESI†).
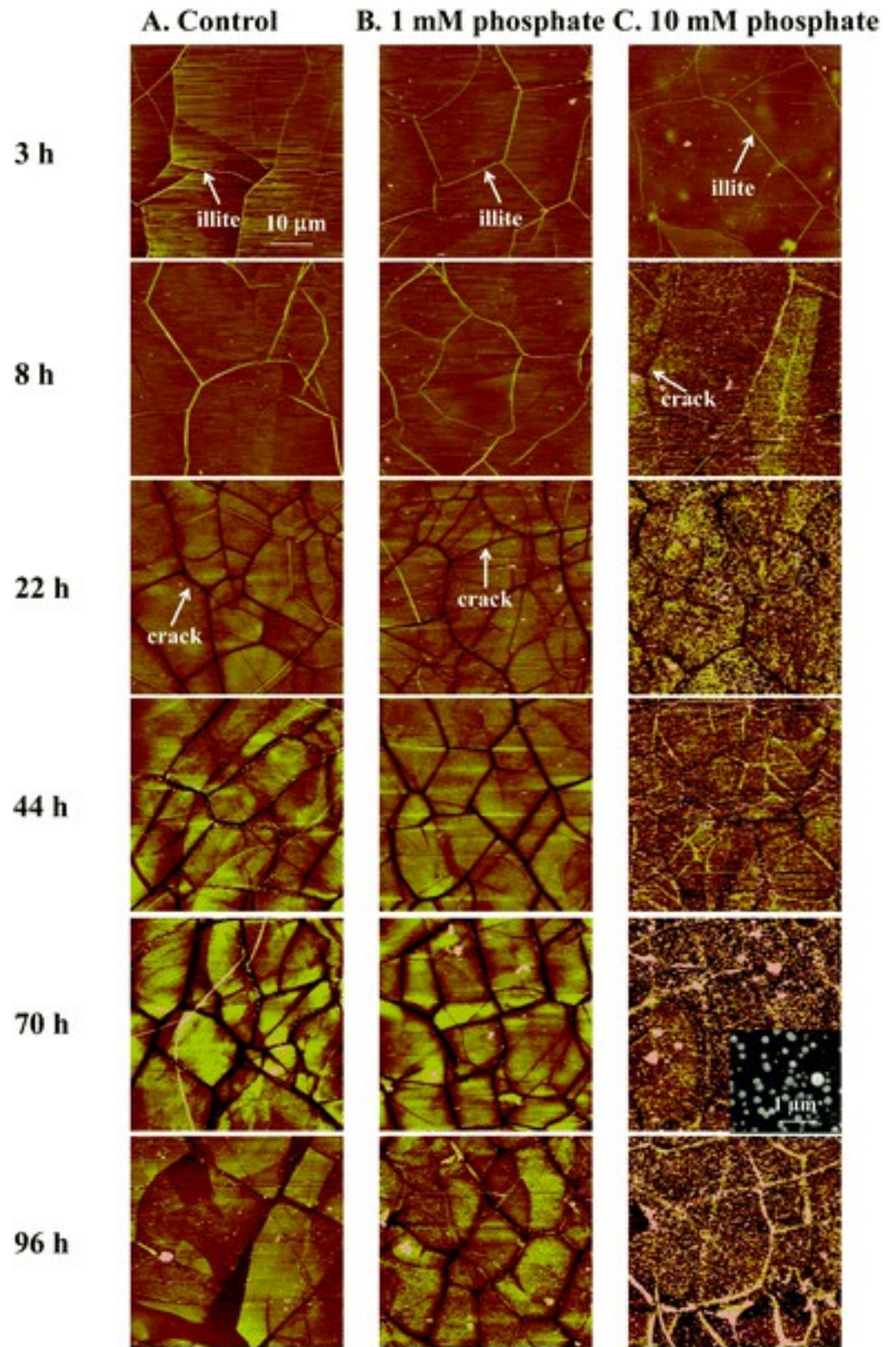
Fig. 2 AFM observations of biotite basal planes after reaction at $T = 95\ °C$ and $P_{CO_2} = 102$ atm with a salinity of initial pH of 3.16 without phosphate (A), with 1 mM phosphate (B), and with 10 mM phosphate (C). AFM imag

By relating microscopic observations to the ICP-OES results, we found that 10 mM phosphate promoted biotite dissolution and consequent secondary precipitation. The surface precipitation of Fe- and Al-bearing phases became more dominant as the reaction time increased, and contributed to lower aqueous concentrations of Fe and Al with 10 mM phosphate than in the control system. Precipitates formed in the 10 mM phosphate solution could also reduce the aqueous Fe and Al concentrations. For the 1 mM phosphate samples, while we could not observe significant precipitation by AFM, secondary precipitation could still have occurred either on biotite surfaces or in the solution, because the results from ICP-OES revealed lower aqueous Fe and Al concentrations. To further investigate phosphate complexation and the phases of secondary precipitates, and to provide additional information to illuminate the mechanisms of phosphate effects, experiments with ATR-FTIR and HR-TEM were conducted.

3.3 Characterization of phosphate surface complexes and secondary mineral phases

ATR-FTIR spectra of phosphate surface complexation are shown in Fig. 3. The spectra for 1 mM phosphate and 10 mM phosphate showed different peaks, suggesting concentration-dependent phosphate complexation with biotite. In previous studies, the peaks at 1080 and 1137 cm^{-1} were assigned to surface precipitates of $AlPO_4$.[33,53] From comparison with the literature, the broad and weak peaks at 1080 cm^{-1} in the 1 mM phosphate spectrum and the peaks at 1074 cm^{-1} in the 10 mM phosphate spectrum (with slight shifts) probably resulted from the formation of surface $AlPO_4$ precipitates. The precipitation could contribute to the lower aqueous Al concentrations observed in both the 1 mM and 10 mM phosphate systems. The peaks at 1007 cm^{-1} and 992 cm^{-1} in the presence of 1.0 mM phosphate are attributed to Fe–PO_4 monodentate mononuclear complexation.[32] More peaks were observed with 10 mM phosphate due to a mixture of surface complexes between phosphate and Al and Fe sites. The peaks at 1105 cm^{-1}, 1015 cm^{-1}, and 985 cm^{-1} are assigned to Al–PO_4 monodentate mononuclear complexation,[33] and peaks at 1015 cm^{-1} and 985 cm^{-1} are also assigned to Fe–PO_4 monodentate mononuclear complexation.[32] Such monodentate mononuclear surface complexation between Fe or/and Al and phosphate can promote the release of Fe and Al, subsequently enhancing the dissolution of Si and Mg.[35,37–39,54] The apparently more numerous and stronger monodentate mononuclear

complexes formed with 10 mM could promote biotite dissolution more significantly than 1 mM phosphate, consistent with ICP-OES results. The enhanced dissolution also could further increase the saturations of secondary minerals and enhance precipitation. There is a caveat to this conclusion, in that the ATR-FTIR analysis was conducted at room temperature and atmospheric pressure. Therefore, the spectra may differ under high temperature and pressure. However, to minimize any potential effects, the initial pH of the ATR-FTIR experiments was adjusted to be 3.16, the same pH as in the biotite dissolution experiments. Thus, although we cannot accurately estimate the potential effects of temperature on phosphate complexation with biotite surface due to a lack of references, the dominant phosphate species in both conditions is $H_2PO_4^-$, because both have the same pH. Furthermore, the ATR-FTIR experimental observations were consistent with the promoted biotite dissolution by 10 mM phosphate. Hence, we expect the general mechanism to be the same under GCS relevant conditions.
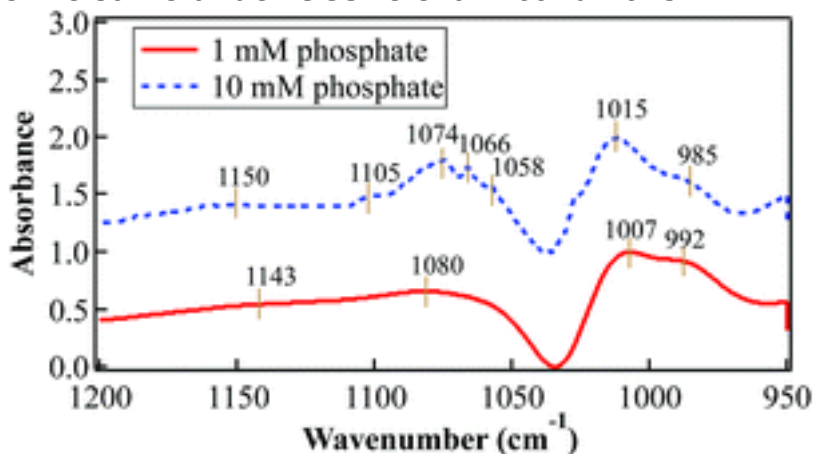
Fig. 3 Normalized ATR-FTIR spectra for biotite contacted with 1 mM (red solid line) and 10 mM (blue dashed line) an ionic strength of 1.0 M and initial pH of 3.16. The spectrum of biotite contacted without phosphate in 1.0 M background and subtracted from the raw spectrum.

Homogeneous precipitation in solution and heterogeneous precipitation on surfaces were observed after reaction with 1 mM and 10 mM phosphate for 22 h, as shown in Fig. 4. The 22 h samples were chosen because we observed lower aqueous concentrations of Al^{3+} with phosphate from that time point on. Samples taken from solutions were amorphous, without obvious electron diffraction patterns observed. EDX analyses (Fig. S7, ESI‡) showed that the precipitated particles were abundant in P and Fe. On the other hand, particles detached from biotite surfaces have clear lattice fringes (Fig. 4A2), and they were identified to be gibbsite (S7 in the ESI‡). Therefore, secondary

mineral precipitation helped reduce aqueous Fe and Al concentrations in the 1 mM and 10 mM systems. After 96 h reaction with 10 mM phosphate, minerals abundant in P, Fe, and Al were observed on the biotite surface (Fig. 4B and Fig. S7, ESI†). By matching the electron diffraction patterns (Table S3, ESI†), we found that the potential secondary precipitates included strengite ($FePO_4 \cdot H_2O$), gibbsite ($Al(OH)_3$), and berlinite ($AlPO_4$). Although the dissolution of biotite was promoted by 10 mM phosphate, secondary precipitation reduced the aqueous Fe and Al concentrations, leading to the lower net Al and Fe concentrations observed by ICP-OES. Obvious promotion effects on biotite dissolution by 10 mM phosphate might also occur, because an excess amount of phosphate was available to remove Al and Fe cations from solution, further promoting the forward dissolution, but not in the 1 mM phosphate system.
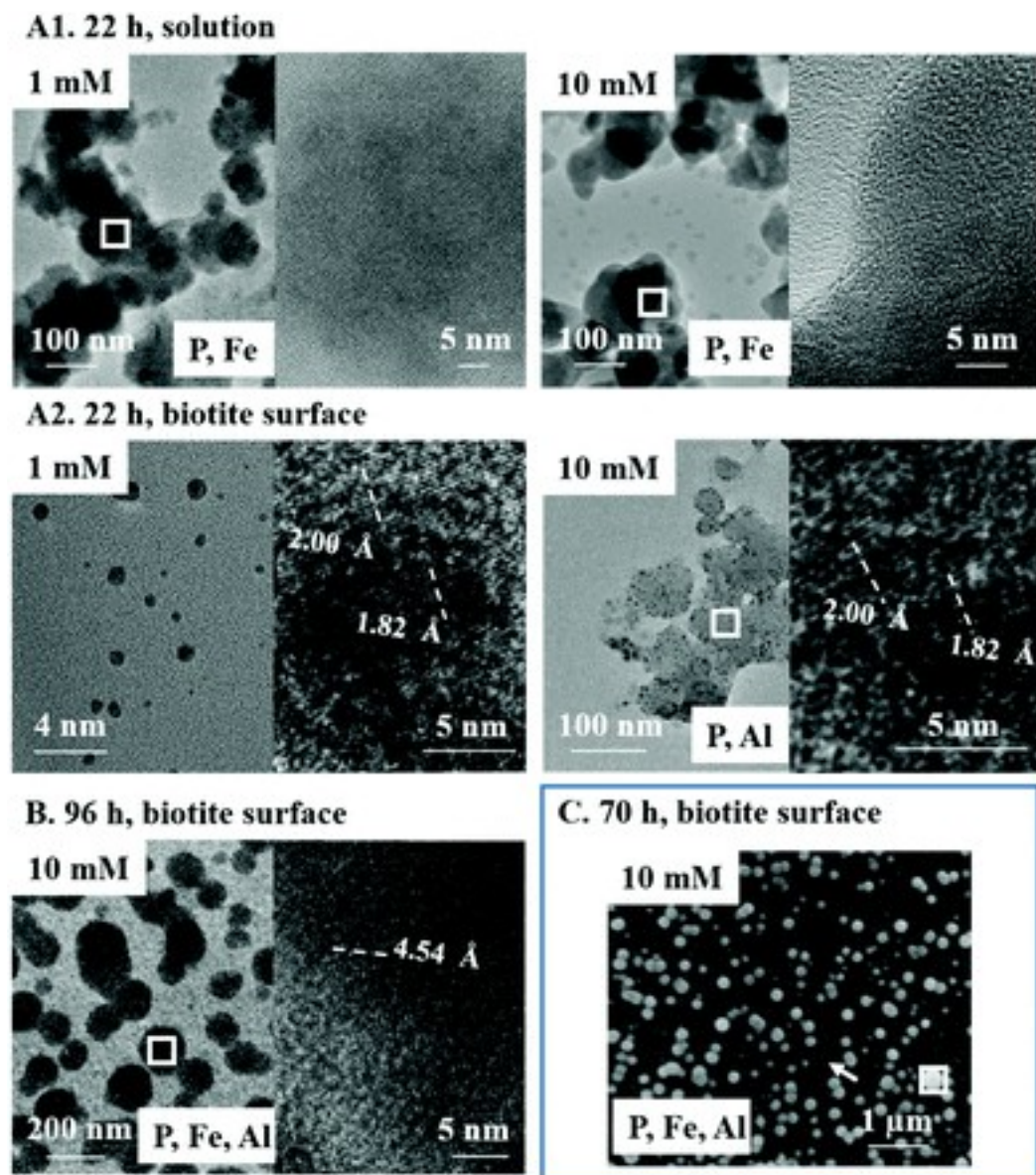
Fig. 4 TEM measurements of samples collected after 22 h reaction with 1 mM or 10 mM phosphate from soluti[...] biotite surface (A2), and collected after 96 h reaction with 10 mM phosphate from biotite surfaces (B); SEM im[...] surface after 70 h reaction with 10 mM phosphate (C), the white arrow points to the thin film. EDX was taken a[...] by the white box, and the abundant elements detected are shown with the images. The white dotted lines show v[...] fringes were observed.

The residual phosphate concentrations after 96 h reaction in the 1 mM phosphate and 10 mM phosphate systems were about 0.7 mM and 9.5 mM, respectively (Fig. S8, ESI†). The decreases of phosphate concentrations in the reaction systems can result from both phosphate adsorption on the biotite surface and precipitation of phosphate minerals. Moreover, the phosphate

concentrations obviously decreased after 44 h reaction, which is consistent with the decrease of aqueous Fe and Al concentrations due to secondary precipitation with phosphate. Therefore, with phosphate, in the first stage (0–40 h for Fe and 0–20 h for Al), dissolution was dominant; then, in the second stage (over a longer time), secondary precipitation of Fe- and Al-bearing phases was predominant over dissolution with higher mineral saturation indices (Table S2, ESI†), reducing the Fe and Al concentrations in the solutions. To investigate how chemical reactions with phosphate alter the wettability of biotite basal surfaces, we conducted contact angle measurements under both ambient conditions and high temperature and pressure conditions.

3.4 Enhanced wettability of biotite basal surfaces by chemical reaction with phosphate

Biotite surface wettability was significantly enhanced after interactions with phosphate, as indicated by contact angles measured under ambient conditions for biotite samples reacted in control, 0.1 mM (a concentration closer to general field site conditions),[25,55] 1 mM, and 10 mM phosphate under 95 °C and 102 atm CO_2 for 70 h (Fig. 5A). For 0.1 and 1 mM phosphate samples, the contact angles were close, but both are lower than control samples. The dissolution extents for samples reacted in the control, 0.1 mM, and 1 mM phosphate systems were similar, and no significant precipitation occurred on these sample surfaces (Fig. 1 and Fig. S9, ESI†). In other words, for these three samples, changes in the surface morphology were not discernible, with similar root-mean-square roughness values (Fig. 5A). Therefore, we conclude that in a low phosphate concentration systems, surface adsorption of phosphate is dominant over dissolution or secondary precipitation in enhancing the biotite surface wettability.

A. Ambient CA measurement
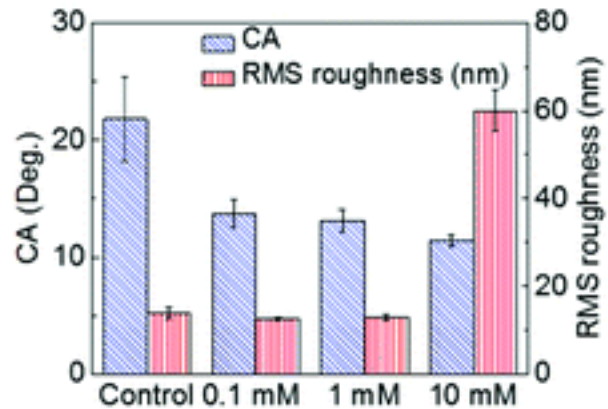
B. High P/T CA measurement

Experimental conditions	Static CA (deg.)	CO$_2$ adhesion	CAH (deg.)	Contact line (mm)
Control	21.1 ± 1.3	Yes	30.7 ± 2.0	1.4 ± 0.2
		No	24.0 ± 1.6	0.6 ± 0.1
10 mM P	14.0 ± 0.6	No	5.6 ± 1.2	0.4 ± 0.1

Fig. 5 Contact angle measurements under ambient conditions (A) and 48 °C and 102 atm CO$_2$ conditions (B) for samples under different phosphate concentrations.

On the other hand, the further slight decrease of contact angles on samples reacted with 10 mM phosphate can be explained by surface precipitation. Surface roughness was much higher for 10 mM phosphate samples than for control, 0.1 mM phosphate, and 1 mM phosphate samples (Fig. 5A). In a recent study by Zhang *et al.*, higher surface roughness, induced by dissolution, enhanced biotite wettability.[15] Similarly, in the present study, a secondary precipitation-induced increase of surface roughness could have also reduced the contact angle on the biotite surface, enhancing its wettability. Second, the chemical identity on the biotite surface changes because of secondary precipitation in the presence of phosphate (S7, ESI†). Hence, newly formed minerals may also affect the wettability because different minerals have their own chemical compositions, crystal structures,

and surface charges.[56] While we could not quantitatively differentiate their roles, we can, therefore, conclude that at a high phosphate concentration both adsorption and significant secondary precipitation can contribute to the enhanced wettability.

To obtain more information on wettability alteration, contact angles for control and 10 mM phosphate samples were measured under high temperature and high pressure conditions (Fig. 5B). The trend was confirmed that the contact angle was lower for 10 mM phosphate sample than that for the control sample. In addition, dynamic wettability was obtained (Fig. S3, ESI†). During withdrawal of CO_2 from the droplet on the mineral surface, both CO_2 adhesion and non-adhesion were observed for the control sample (S3 in the ESI†), as reported in our recent study.[15] However, CO_2 easily detached from the mineral surface during withdrawal, and did not show any adhesion on the 10 mM phosphate sample. The enhanced surface wettability after reaction with 10 mM phosphate reduced the incidence of CO_2 adhesion. The length of the contact line, the ternary phase line among biotite, CO_2, and brine, was measured at the last moment of the CO_2 withdrawal process. The contact line was longer when there was CO_2 adhesion for the control sample (Fig. 5B), suggesting that it was pinned (or stuck) on the mineral surface. Contact angle hysteresis (CAH), defined as the difference between the minimum water contact angle when injecting CO_2 into the droplet on the mineral surface and the maximal water contact angle when withdrawing CO_2 from the droplet, acts as an indicator of residual trapping capacity during drainage and rewetting processes.[45] The observed CAH was lower when there was no CO_2 adhesion for both the control and 10 mM phosphate samples, and the CAH on the 10 mM phosphate sample was even lower than on the control sample. Therefore, CO_2 adhesion contributed to a longer contact line and higher CAH. This information can help us better understand

CO_2 migration and storage in sequestration sites: the enhanced wettability and reduced CO_2 adhesion with phosphate can help CO_2 move more freely, and the decreased CAH indicates a lower residual trapping capacity of CO_2.

4. Conclusions

In this study, for the first time, we systematically report the concentration-dependent effects of phosphate on biotite dissolution and element-specific secondary precipitation. A higher concentration of phosphate (10 mM) promoted biotite dissolution, and low concentrations of phosphate did not greatly affect biotite dissolution. However, in the presence of phosphate, even at 0.1 mM, phosphate precipitated with Fe and Al as secondary minerals both at biotite surfaces and in the aqueous solutions, reducing aqueous Fe and Al concentrations. Secondary precipitation may block pores in subsurface sites, thus reducing their porosity and permeability. Furthermore, we show the consequent surface morphology evolution and alteration of wettability of biotite under conditions relevant to subsurface sites, information which could not be obtained through simulations alone. Biotite wettability was significantly promoted by the presence of phosphate, which was effective even in 0.1 mM phosphate and this was mainly due to phosphate adsorption. Wettability is a key factor determining the distribution and transport of fluids in subsurface sites. Therefore, the new findings about the effects of phosphate on the interfacial reactions of minerals and their subsequent physicochemical property changes can contribute to safe and efficient geologic CO_2 sequestration. In addition, the information about the phosphate effects can benefit our understanding of other processes where physical chemistry of phosphate is critically involved, such as other engineered subsurface processes or material fabrication.

Conflicts of interest

There are no conflicts to declare.

Acknowledgements

References

1. B. Metz, O. Davidson, H. De Coninck, M. Loos and L. Meyer, *IPCC special report on carbon dioxide capture and storage: Prepared by Working Group III of the Intergovernmental Panel on Climate Change*, IPCC, Cambridge University Press, Cambridge, United Kingdom and New York, USA, 2005 Search PubMed.
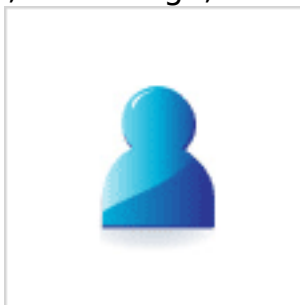
2. L. W. Lake, *Enhanced oil recovery*, Prentice Hall, Englewood Cliffs, NJ, 1989 Search PubMed.

3. R. G. Bruant, M. A. Celia, A. J. Guswa and C. A. Peters, Safe Storage of CO_2 in Deep Saline Aquifiers, *Environ. Sci. Technol.*, 2002, **36**(11), 240A–245A CrossRef CAS PubMed.
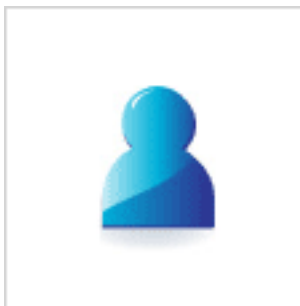
4. F. M. Orr, Onshore geologic storage of CO_2, *Science*, 2009, **325**(5948), 1656–1658 CrossRef CAS PubMed.
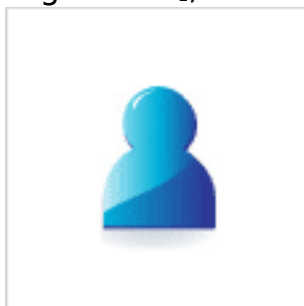
5. T. K. Tokunaga, DLVO-based estimates of adsorbed water film thicknesses in geologic CO_2 reservoirs, *Langmuir*, 2012,**28**(21), 8001–8009 [CrossRef] [CAS] [PubMed] .
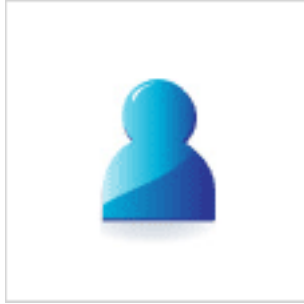
6. P. Bondor, Applications of carbon dioxide in enhanced oil recovery, *Energy Convers. Manage.*, 1992, **33**(5), 579–586 [CrossRef] [CAS] .

7. Y.-S. Jun, D. E. Giammar and C. J. Werth, Impacts of geochemical reactions on geologic carbon sequestration,*Environ. Sci. Technol.*, 2013, **47**(1), 3–8 [CrossRef] [CAS] [PubMed] .
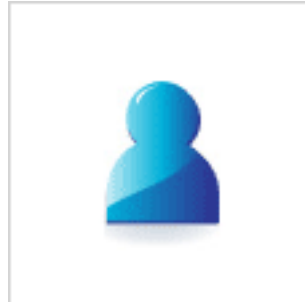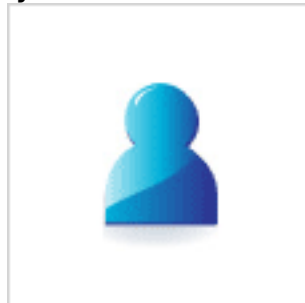
8. T. K. Tokunaga and J. Wan, Capillary pressure and mineral wettability influences on reservoir CO_2 capacity, *Rev. Mineral. Geochem.*, 2013, **77**(1), 481–503 [CrossRef] [CAS] .

9. R. S. Middleton, G. N. Keating, P. H. Stauffer, A. B. Jordan, H. S. Viswanathan, Q. J. Kang, J. W. Carey, M. L. Mulkey, E. J. Sullivan and S. P. Chu, The cross-scale science of CO_2 capture and storage: from pore

scale to regional scale, *Energy Environ. Sci.*, 2012, **5**(6), 7328–

7345 CAS .

10. J. S. Ellis and A. Bazylak, Dynamic pore network model of surface heterogeneity in brine-filled porous media for carbon sequestration, *Phys. Chem. Chem. Phys.*, 2012, **14**(23), 8382–

8390 RSC .

11. Y. Hu and Y. S. Jun, Biotite dissolution in brine at varied temperatures and CO_2 pressures: its activation energy and potential CO_2 intercalation, *Langmuir*, 2012, **28**(41), 14633–

14641 CrossRef CAS PubMed .

12. H. Shao, J. R. Ray and Y.-S. Jun, Effects of salinity and the extent of water on supercritical CO_2-induced phlogopite dissolution and secondary mineral formation, *Environ. Sci. Technol.*, 2011, **45**(4),

1737–1743 CrossRef CAS PubMed .

13. R. J. Rosenbauer, T. Koksalan and J. L. Palandri, Experimental investigation of CO_2–brine–rock interactions at elevated temperature and pressure: implications for CO_2 sequestration in deep-saline aquifers, *Fuel Process. Technol.*, 2005, **86**(14), 1581–1597 CrossRef CAS .
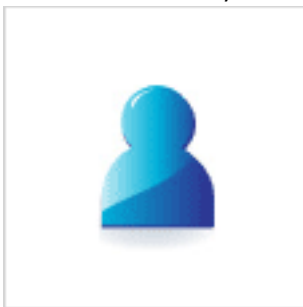
14. L. Zhang and Y.-S. Jun, Distinctive Reactivities at Biotite Edge and Basal Planes in the Presence of Organic Ligands: Implications for Organic-Rich Geologic CO_2 Sequestration, *Environ. Sci. Technol.*, 2015, **49**(16), 10217–10225 CrossRef CAS PubMed .
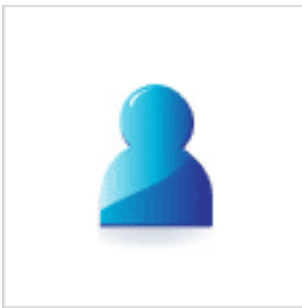
15. L. Zhang, Y. Kim, H. Jung, J. Wan and Y.-S. Jun, Effects of Salinity-Induced Chemical Reactions on Biotite Wettability Changes under Geologic CO_2 Sequestration Conditions, *Environ. Sci. Technol. Lett.*, 2016, **3**(3), 92–97 CrossRef CAS .

16. Y. Yang, Y. Min and Y.-S. Jun, A mechanistic understanding of plagioclase dissolution based on Al occupancy and T–O bond length: from geologic

carbon sequestration to ambient conditions, *Phys. Chem. Chem. Phys.*, 2013, **15**(42), 18491–18501 RSC .
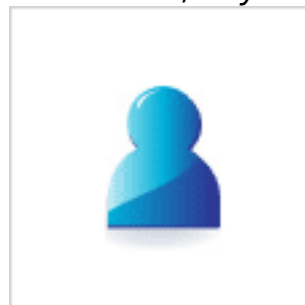
17. Y.-S. Jun, L. Zhang, Y. Min and Q. Li, Nanoscale Chemical Processes Affecting Storage Capacities and Seals during Geologic CO_2 Sequestration, *Acc. Chem. Res.*, 2017, **50**(7), 1521–1529 CrossRef CAS PubMed .

18. D. R. Cole, A. A. Chialvo, G. Rother, L. Vlcek and P. T. Cummings, Supercritical fluid behavior at nanoscale interfaces: implications for CO_2 sequestration in geologic formations, *Philos. Mag.*, 2010, **90**(17–18), 2339–2363 CrossRef CAS .
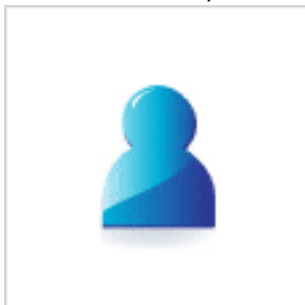
19. C. A. Griffith, D. A. Dzombak and G. V. Lowry, Physical and chemical characteristics of potential seal strata in regions considered for demonstrating geological saline CO_2 sequestration, *Environ. Earth Sci.*, 2011, **64**(4), 925–948 CrossRef CAS .

20. H. Shao and Y. S. Jun, Mineral dissolution and nanoparticle evolution on phlogopite surfaces under CO_2 geologic sequestration conditions, *Geochim. Cosmochim. Acta*, 2010, **74**(12), A940–

A940 [Search PubMed] .

21. J. Wan, Y. Kim and T. K. Tokunaga, Contact angle measurement ambiguity in supercritical CO_2–water–mineral systems: mica as an example, *Int. J. Greenhouse Gas Control*, 2014, **31**, 128–

137 [CrossRef] [CAS] .

22. P. Chiquet, D. Broseta and S. Thibeau, Wettability alteration of caprock minerals by carbon dioxide, *Geofluids*, 2007, **7**(2), 112–

122 [CrossRef] [CAS] .

23. Y. K. Kharaka, J. J. Thordsen, S. D. Hovorka, H. Seay Nance, D. R. Cole, T. J. Phelps and K. G. Knauss, Potential environmental issues of CO_2 storage in deep saline aquifers: geochemical results from the Frio-I

Brine Pilot test, Texas, USA, *Appl. Geochem.*, 2009, **24**(6), 1106–

1112 CrossRef CAS .

24. S. J. Keller, *Analyses of subsurface brines of Indiana*, State of Indiana, Department of Natural Resources, Geological Survey,
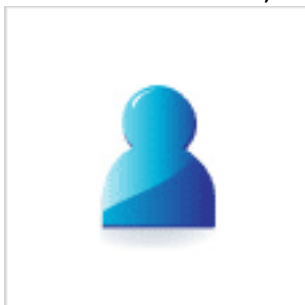
1983 Search PubMed .

25. J. J. Thordsen, Y. K. Kharaka, G. Ambats, E. Kakouros and M. M. Abbott, *Geochemical Data from Produced Water Contamination Investigations: Osage-Skiatook Petroleum Environmental Research (OSPER) Sites, Osage County, Oklahoma*, DTIC Document, 2007.

26. Y. Yang, C. Ronzio and Y.-S. Jun, The effects of initial acetate concentration on CO_2–brine–anorthite interactions under geologic CO_2 sequestration conditions, *Energy Environ. Sci.*, 2011, **4**(11), 4596–

4606 CAS .

27. C. Luengo, M. Brigante, J. Antelo and M. Avena, Kinetics of phosphate adsorption on goethite: comparing batch adsorption and ATR-IR

measurements, *J. Colloid Interface Sci.*, 2006, **300**(2), 511–
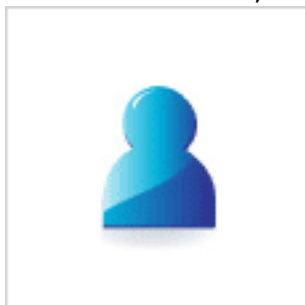
518 CrossRef CAS PubMed .

28. K. D. Kwon and J. D. Kubicki, Molecular orbital theory study on surface complex structures of phosphates to iron hydroxides: calculation of vibrational frequencies and adsorption energies, *Langmuir*,
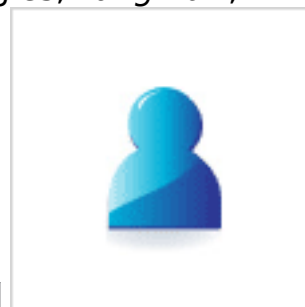
2004, **20**(21), 9249–9254 CrossRef CAS PubMed .

29. T. J. Van Emmerik, D. E. Sandström, O. N. Antzutkin, M. J. Angove and B. B. Johnson, 31P solid-state nuclear magnetic resonance study of the sorption of phosphate onto gibbsite and kaolinite, *Langmuir*,
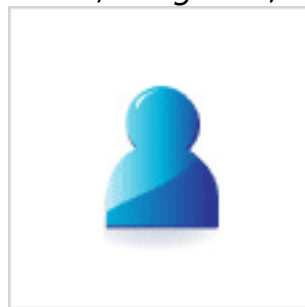
2007, **23**(6), 3205–3213 CrossRef CAS PubMed .

30. O. H. Hsu, Fixation of phosphate by aluminum and iron acidic soils, *Soil*
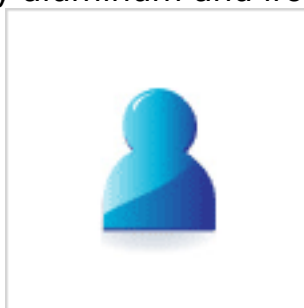
Sci., 1965, **99**(6), 398–402 CrossRef .

31. S. Chang and M. Jackson, Solubility product of iron phosphate, *Soil Sci. Soc. Am. J.*, 1957, **21**(3), 265–269 [CrossRef] [CAS].

32. M. I. Tejedor-Tejedor and M. A. Anderson, The protonation of phosphate on the surface of goethite as studied by CIR-FTIR and electrophoretic mobility, *Langmuir*, 1990, **6**(3), 602–611 [CrossRef] [CAS].
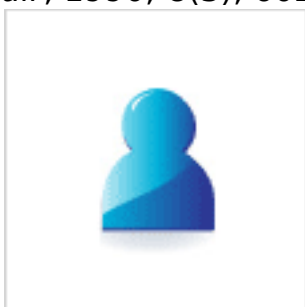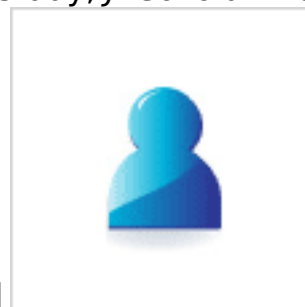
33. T.-T. Zheng, Z.-X. Sun, X.-F. Yang and A. Holmgren, Sorption of phosphate onto mesoporous γ-alumina studied with *in situ* ATR-FTIR spectroscopy, *Chem. Cent. J.*, 2012, **6**, 26 [CAS].
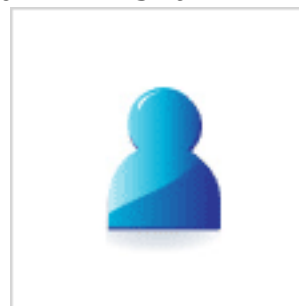
34. C. Luengo, M. Brigante and M. Avena, Adsorption kinetics of phosphate and arsenate on goethite. A comparative study, *J. Colloid Interface Sci.*, 2007, **311**(2), 354–360 [CrossRef] [CAS] [PubMed].
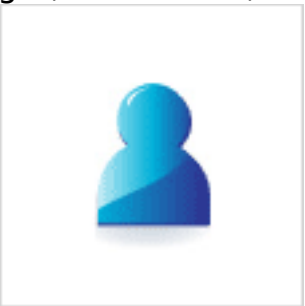
35. M. V. Biber, M. dos Santos Afonso and W. Stumm, The coordination chemistry of weathering: IV. Inhibition of the dissolution of oxide

minerals, *Geochim. Cosmochim. Acta*, 1994, **58**(9), 1999–

2010 CrossRef CAS .

36. S. L. Brantley, J. D. Kubicki and A. F. White, *Kinetics of water-rock interaction*, Springer, Menlo Park, USA,

2008 Search PubMed .

37. W. Stumm and G. Furrer, The dissolution of oxides and aluminum silicates; examples of surface-coordination-controlled kinetics, in *Aquatic Surface Chemistry: Chemical Processes at the Particle-Water Interface*, ed. W. Stumm, John Wiley and Sons, 1987, pp. 197–

219 Search PubMed .

38. W. Stumm, G. Furrer, E. Wieland and B. Zinder, The effects of complex-forming ligands on the dissolution of oxides and aluminosilicates, *The chemistry of weathering*, Springer, 1985, pp. 55–

74 Search PubMed .

39. G. Bondietti, J. Sinniger and W. Stumm, The reactivity of Fe(III)(hydr) oxides: effects of ligands in inhibiting the dissolution, *Colloids Surf., A*, 1993, **79**(2), 157–167 CrossRef .
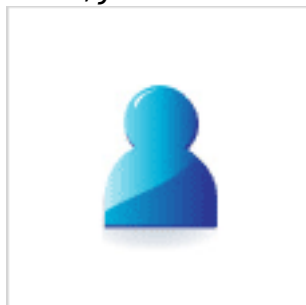
40. P. Zhang, D. Shen, G. Ruan, A. T. Kan and M. B. Tomson, Mechanistic understanding of calcium–phosphonate solid dissolution and scale inhibitor return behavior in oilfield reservoir: formation of middle phase, *Phys. Chem. Chem. Phys.*, 2016, **18**(31), 21458–21468 RSC .

41. F. Yan, F. Zhang, N. Bhandari, L. Wang, Z. Dai, Z. Zhang, Y. Liu, G. Ruan, A. Kan and M. Tomson, Adsorption and precipitation of scale inhibitors on shale formations, *J. Pet. Sci. Eng.*, 2015, **136**, 32–40 CrossRef CAS .

42. B. Nowack, Environmental chemistry of phosphonates, *Water Res.*, 2003, **37**(11), 2533–2546 CrossRef CAS PubMed .

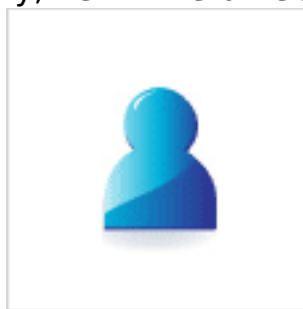43. S. Kononova and M. Nesmeyanova, Phosphonates and their degradation by microorganisms, *Biochemistry*, 2002,**67**(2), 184–195 CAS .

44. K. D. Demadis and A. Ketsetzi, Degradation of Phosphonate-Based Scale Inhibitor Additives in the Presence of Oxidizing Biocides:"Collateral Damages" in Industrial Water Systems, *Sep. Sci. Technol.*, 2007, **42**(7), 1639–1649 CrossRef CAS .

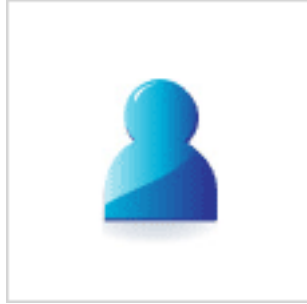45. T. K. Tokunaga and J. Wan, Capillary pressure and mineral wettability influences on reservoir CO_2 capacity, *Rev. Mineral. Geochem.*, 2013, **77**(1), 481–503 CrossRef CAS .

46. W. J. Harrison and L. L. Summa, Paleohydrology of the Gulf of Mexico basin, *Am. J. Sci.*, 1991, **291**(2), 109–176 CrossRef .

47. S. J. Keller, *Analyses of subsurface brines of Indiana*, State of Indiana, Department of Natural Resources, Geological Survey, Bloomington, 1983 [Search PubMed].

48. S. Emberley, I. Hutcheon, M. Shevalier, K. Durocher, B. Mayer, W. Gunter and E. Perkins, Monitoring of fluid–rock interaction and CO_2 storage through produced fluid sampling at the Weyburn CO_2-injection enhanced oil recovery site, Saskatchewan, Canada, *Appl. Geochem.*, 2005, **20**(6), 1131–1157 [CrossRef] [CAS].

49. Y. Hu, J. R. Ray and Y. S. Jun, Biotite–brine interactions under acidic hydrothermal conditions: fibrous illite, goethite, and kaolinite formation and biotite surface cracking, *Environ. Sci. Technol.*, 2011, **45**(14), 6175–6180 [CrossRef] [CAS] [PubMed].

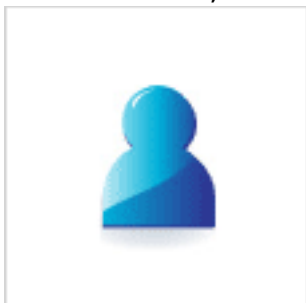50. Y. Hu, J. R. Ray and Y. S. Jun, Na^+, Ca^{2+}, and Mg^{2+} in brines affect supercritical CO_2–brine–biotite interactions: ion exchange, biotite

dissolution, and illite precipitation, *Environ. Sci. Technol.*, 2013, **47**(1),
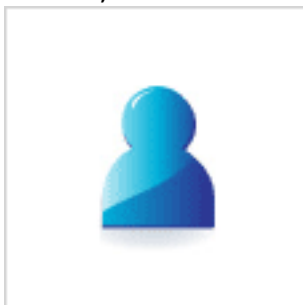
191–197 CrossRef CAS PubMed .

51. J. Bradshaw and P. Cook, Geological sequestration of carbon dioxide, *Environ. Geosci.*, 2001, **8**(3), 149–
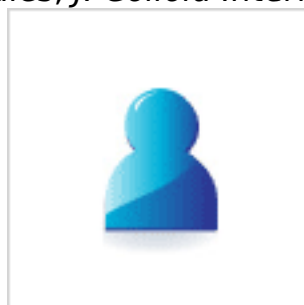
151 CrossRef .

52. E. Gadelmawla, M. Koura, T. Maksoud, I. Elewa and H. Soliman, Roughness parameters, *J. Mater. Process. Technol.*, 2002, **123**(1), 133–

145 CrossRef .

53. M. Del Nero, C. Galindo, R. Barillon, E. Halter and B. Madé, Surface reactivity of α-Al$_2$O$_3$ and mechanisms of phosphate sorption: *in situ* ATR-FTIR spectroscopy and ζ potential studies, *J. Colloid Interface*

Sci., 2010, **342**(2), 437–444 CrossRef CAS PubMed .

54. W. Stumm and J. J. Morgan, *Aquatic chemistry: chemical equilibria and rates in natural waters*, John Wiley & Sons, 2012, vol.

126 [Search PubMed] .

55. B. C. Bostick, S. Fendorf, M. O. Barnett, P. M. Jardine and S. C. Brooks, Uranyl surface complexes formed on subsurface media from DOE facilities, *Soil Sci. Soc. Am. J.*, 2002, **66**(1), 99–

108 [CrossRef] [CAS] .

56. S. Barclay and R. Worden, Effects of reservoir wettability on quartz cementation in oil fields, in *Quartz cementation in sandstones*, ed. R. Worden and S. Morad, Blackwell Science Ltd, 2000, vol. 29, pp. 103–

117 [Search PubMed] .